Student Conference Proceedings
Vol 2, No 1, 2026, Article ID 2706, 4 Pages

Student Conference Lübeck

Proceedings Article

Sub-Frame Chebyshev Reconstruction for Magnetic Particle Imaging

Daniela Hilbert [a*] · Marco Maass [b] · Marcin Grzegorzek [b,c*]

[a] Study program Medical Engineering Science, Universität zu Lübeck, Lübeck, Germany
[b] German Research Center for Artificial Intelligence (DFKI), Lübeck, Germany
[c] Institute of Medical Informatics, Universität zu Lübeck, Lübeck, Germany
[*] Corresponding author, email: daniela.hilbert@student.uni-luebeck.de; marcin.grzegorzek@uni-luebeck.de

Received 17 February 2026; Accepted 03 July 2026; Published online 13 July 2026

Abstract

Magnetic Particle Imaging typically performs image reconstruction only after the full measurement has been acquired. This work investigates whether partial reconstructions during an ongoing measurement can be advantageous when only sets of sub-frames of the acquired signal are used. Static particle concentrations and their corresponding voltage signals were simulated, segmented using Hann windows, and reconstructed via direct Chebyshev reconstruction followed by kernel-based deconvolution, and cumulative reconstructions were obtained by summing the sub-frame results. The results show that reconstruction quality depends strongly on the regularization parameter and the information content of the selected sub-frames. For large regularization values, the full signal yielded the lowest error, whereas for sufficiently small regularization parameters, certain window configurations outperformed the full-signal reconstruction. These findings suggest that selectively excluding low-information sub-frames may improve reconstruction stability and reduce computational effort.

I. Introduction

Magnetic Particle Imaging (MPI) is a tracer-based imaging modality that exploits the nonlinear magnetization response of superparamagnetic nanoparticles in a dynamic magnetic field. These tracers enable both static applications, such as tumor detection [1], and dynamic tasks like blood-flow imaging or instrument tracking [2]. An oscillating excitation field induces magnetization changes that are detected as voltage signals in the receive coils.

Spatial encoding is achieved by an additional static, spatially inhomogeneous selection field that creates a field-free point (FFP). Particles far from the FFP are saturated by the selection field and therefore do not contribute to the signal when the excitation field is applied. Only particles in the vicinity of the FFP experience a change in magnetization caused by the excitation field and thus induce a voltage in the receive coils. To scan the entire field of view (FOV), the FFP is moved non-mechanically. This can be achieved either by increasing the amplitude of the excitation field or by applying an additional homogeneous magnetic field, the drive field.

Increasing the selection field amplitude is avoided in practice due to peripheral nerve stimulation. The drive field shifts the FFP along a trajectory, often a Lissajous pattern, through superposition with the selection field. Knowing the spatial positions of the FFP enables spatial encoding, as the measured voltage signals can be assigned to corresponding spatial locations.

Due to the fast movement of the FFP, in which the physical effect of changing magnetization occurs, through the FOV, the particle magnetization changes at high frequencies. As a result of the dynamic processes happening inside the FOV, the voltage signals exhibit fast temporal dynamics. Consequently, high temporal resolution is required during measurement to avoid motion artefacts and distortions in the raw data [3].

High temporal resolution is also essential during image reconstruction. This is due to spatial encoding in MPI which relies on the assignment of the measured signal to the FFP position. If resolution at reconstruction is insufficient, the assignment of signal and position becomes inaccurate. Motion artefacts and spatial blurring can be seen.

In most reconstruction methods, image computation starts only after a completed acquistion of a frame, meaning that the FFP has traversed the full trajectory within the FOV. This applies to a variety of reconstruction techniques, including frequency-domain approaches such as the direct Chebyshev reconstruction (DCR) used in this work [4]. In practice not all parts of the acquired signal, so called sub-frames, necessarily contribute equally to the reconstruction quality. In particular, sub-frames in which the FFP passes regions with little or no particle concentration may add noise rather than information. Only a few approaches have investigated how reconstruction behaves when only parts of the acquired signal are used, such as in [5]. In this work, it was therefore investigated how using only subsets of the measured signal affects the reconstruction.

II. Methods and materials

In the following section, the basic principles of image reconstruction are briefly explained, especially the in this case used DCR and kernel-based deconvolution. The methods used to window the signals and to compare the different reconstructed images are described in detail as well.

II.I. Basic principles of image reconstruction

The temporal signal is mapped to spatial positions to form the system matrix $S \in \mathbb{R}^{N_t \times N_p}$, where N_t denotes the number of measurement time steps and N_p the number of pixels, or voxels in three-dimensional imaging. Since the system matrix describes how particle concentration at each position contributes to the measured voltage, signal generation can be expressed by the linear forward model

$$Sc = u, \tag{1}$$

where $c \in \mathbb{R}^{N_p}$ represents the unknown particle concentration and $u \in \mathbb{R}^{N_t}$ the measured voltage signal.

With this linear forward model, the inverse problem consists of recovering the unknown concentration c from the acquired data u. One reconstruction approach is the DCR, an analytical, model-based method operating in the frequency domain. It relies on the simplified Langevin model of paramagnetism, combined with several additional approximations. The concentration distribution is modeled as a convolution of the particle response with the system kernel. Therefore the convolved particle concentration can be written equally to [4] as

$$\tilde{c}(x) = \big(c(z) * \mathscr{L}_{z_1,z_2}(-\beta G z)\big)\big(G^{-1}Ax\big), \tag{2}$$

where $\mathscr{L}_{z_1,z_2}$ denotes the partial derivative of the two-dimensional Langevin function, $G \in \mathbb{R}^{2\times 2}$ and $A \in \mathbb{R}^{2\times 2}$ are matrices containing the gradients and amplitudes of the magnetic fields and $\beta \in \mathbb{R}$ is a known constant. This convolution is in the DCR [4] then approximated by

$$\begin{aligned}\tilde{c}(x) \approx \sum_{k\in\mathbb{K}} &\frac{4\left|\big(k-\lambda_k^* N_B\big)\big(k-\lambda_k^*(N_B-1)\big)\right|}{\pi^2\beta^2 \det(A)} (C_k)^{-1} \\ &\hat{u}_k \mathrm{i}^{\lambda_k^*} U_{|n_k^*|-1}(x_1) U_{|m_k^*|-1}(x_2),\end{aligned} \tag{3}$$

with the set $\mathbb{K}$ containing for the sum relevant frequency components, $\lambda_k^* = \mathrm{round}\Big(\frac{(2N_B-1)k}{(2N_B^2-2N_B-1)}\Big)$ and N_B the frequency divider of the excitation. $C_k \in \mathbb{R}^{2\times 2}$ is a matrix that combines various physical coefficients. After Fourier-transforming the measured voltage signal, $\hat{u}_k$ describes its k-th frequency component, while $U_n : \mathbb{R} \to \mathbb{R}$ are Chebyshev polynomials of second kind and order $n \in \mathbb{N}$. These approximations enable a direct computation of the concentration distribution and eliminate the need for an explicitly measured system matrix, whose acquisition is time-consuming.

The obtained concentration estimate still contains blurring effects caused by the system's point-spread function. To compensate for this, a kernel-based deconvolution is applied. The deconvolution is typically formulated as a regularized inverse problem and reconstructs the particle concentration c by solving a regularized least-squares problem of the form

$$\underset{c\in\mathbb{R}^{N_p}}{\arg\min} \left\| K\mathscr{F}(c) - \tilde{C}\right\|_2^2 + \lambda \|c\|_2^2 \tag{4}$$

with the regularization parameter λ. The expression $\mathscr{F}$ describes the operator for the discrete Fourier transform. The matrix $K = (K_1,\ K_2)^T$ contains two diagonal matrices, each with the Fourier transform of the elements of the convolution kernel. The Fourier transform of the approximated reconstructed particle concentration is given by the image matrix $\tilde{C}$ which contains the concentration for both receive coils. This refinement step improves spatial resolution and yields a more accurate reconstruction of the underlying particle distribution.

II.II. Methods

To investigate the effect of reduced measurement duration on reconstruction quality, the fully sampled signal was modified using element-wise windowing with varying window lengths, overlaps and starting positions. Each windowed and then Fourier-transformed signal was reconstructed using the DCR method and the kernel-based deconvolution approach, and the resulting images were compared to the reconstruction obtained from

DOI 10.18416/SCP.2026.2706

the complete measurement using an error metric. In a second step, sub-frames were added cumulatively to the measurement, and each intermediate reconstruction was again evaluated against the fully sampled reference. This procedure enabled a systematic analysis of how image quality depends on the fraction of the measurement signal that is available.

II.III. Implementation

In this work, only simulated and noise-free data was used. To synthesize the voltage signals, a system matrix for each receive coil was computed based on appropriate physical parameters. The diameter of the superparamagnetic tracer particles was set to 22 nm. The gradients of the selection field, were chosen as $G_x = G_y = -1\,\mathrm{T/m}\mu_0$ and $G_z = 2\,\mathrm{T/m}\mu_0$ with $\mu_0 = 1.257 \cdot 10^{-6}\,\mathrm{H\,m^{-1}}$ denoting the magnetic field constant. The excitation field was defined using amplitudes $A_x = A_y = 0.12\,\mathrm{mT}/\mu_0$, $A_z = 0\,\mathrm{mT}/\mu_0$ and an excitation frequency ratio of $\frac{f_x}{f_y} = \frac{N_B-1}{N_B}$, $N_B = 33$. Using this ratio and a base frequency of $f_B = 0.833$ MHz, the duration of one complete trajectory is given by $T_D = 1.3$ ms. A sampling rate of $f_s = \frac{N_t}{T_D} = 6.3015$ MHz was used with $N_t = 8192$ time steps. The FOV was 24 mm× 24 mm with an image resolution of 81 × 81 pixels and a pixel size of 0.2963 × 0.2963 mm. This yields a total number of pixels of $N_p = 81 \cdot 81 = 6561$.

The voltage signals were simulated using a known ground truth concentration c, also called the phantom, by (1). The used phantom can be seen in Fig. 1.

As window function a symmetric Hann window of the form

$$w(n) = 0.5 - 0.5\cos\left(\frac{2\pi n}{L-1}\right), \quad n = 0, 1, \ldots, L-1 \tag{5}$$

with window length L was used. To test different sizes, the window length was chosen from $L \in \{128, 256, 512, 1024, 2048, 4096, 8192\}$. With the trajectory duration T_D, these lengths equal a measurement time of $t_w \in \{0.0203\,\mathrm{ms}, 0.0406\,\mathrm{ms}, 0.0813\,\mathrm{ms}, 0.1625\,\mathrm{ms}, 0.325\,\mathrm{ms}, 0.65\,\mathrm{ms}, 1.3\,\mathrm{ms}\}$. The windows were applied with an overlap of half the window size. Since the Hann window is constructed such that two windows shifted by half their length sum to one, the procedure introduces no reconstruction error.

As most window lengths are smaller than the signal length, zero padding the window to the length of the voltage signal was required to enable the element-wise multiplication of the signal and the window function. This procedure allows the use of windows for different sub-frames as well as multiple starting points of the first sub-frame.

After zero padding, for both coils the windowed voltage signal u_j, with $j \in \mathbb{N}$ being the window number, was obtained by element-wise multiplication of the voltage u and the window w_j. Each windowed voltage signal was then transformed into the frequency domain using a Fast Fourier Transform (FFT). The FFT was computed with a length of N_t samples. To reconstruct the windowed signals in the frequency domain, the DCR was applied to every sub-frame individually. For this, the set $\mathbb{K}$ was defined as $\mathbb{K} = \{k \in \{62, ..., 500\} | n_k^* \neq 0, m_k^* \neq 0\}$. The frequency components with $k \in \{0, 1, \ldots, 61\}$ are discarded because in real measurements these frequencies are strongly affected by the excitation field and the actual particle signal is therefore severely distorted. The reconstruction was performed using (3) with $n_k^* = -k + \lambda_k^* N_B$ and $m_k^* = k - \lambda_k^*(N_B - 1)$.

With the Fourier transform $\tilde{C}_j$ of the obtained approximated particle concentration, the minimization problem in (4) was solved analytically by

$$c_j = \mathscr{F}^{-1}\left(\left(K^H K + \mu I\right)^{-1} K^H \tilde{C}_j\right), \tag{6}$$

where $\mu \in \mathbb{P}$ denotes the regularization parameter with $\mathbb{P} = \{10^n \mid n \in \{-12, -11, \ldots, 12\}\}$ and $I \in \mathbb{R}^{N_p \times N_p}$ is the identity matrix.

To analyse the required level of signal coverage, the reconstructed images of the single sub-frames were added successively to obtain

$$c^l = \sum_{j=1}^{l} c_j, \quad l \in \left\{1, 2, \ldots, \frac{2N_t}{L}\right\}. \tag{7}$$

After the summation, the final step for reconstruction was to set all negative elements of c^l to zero as there cannot exist negative particle concentration. The intermediate results were compared with the ground truth after each summation. In this case the Mean Absolute Error (MAE), defined as

$$e_{\mathrm{MAE}} = \frac{1}{N_p} \sum_{i=1}^{N_p} \left| c^l(i) - c(i) \right| \tag{8}$$

with $c^l \in \mathbb{R}^{N_p}$ the vectorized summed concentration estimate by (7) and $c \in \mathbb{R}^{N_p}$ the vectorized ground truth concentration, was used to objectively evaluate the reconstruction quality.

III. Results and discussion

The visual reconstruction quality of the employed phantom was generally limited for the chosen parameter configuration. This can be observed in Fig. 1 where the reconstruction of the phantom is shown for using a window length $L = 8192$. For this reason, the following analysis focuses primarily on objective error metrics rather than qualitative visual comparisons.

It was observed that for regularization parameters of $\lambda \geq 10^5$, the error metric no longer changed noticeably, independent of the window lengths or the starting position of the first window. This can be seen in Fig. 2.

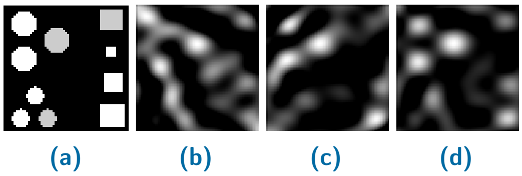

Figure 1: (a) The used phantom describing the ground truth particle concentration with the black pixels representing a concentration of zero and increasing brightness corresponding to higher concentrations. (b) Reconstruction using first sub-frame with $L = 8192$ and $\lambda = 10^1$. (c) Reconstruction using second sub-frame with $L = 8192$ and $\lambda = 10^1$. (d) Cumulative reconstruction using both sub-frames with $L = 8192$ and $\lambda = 10^1$.

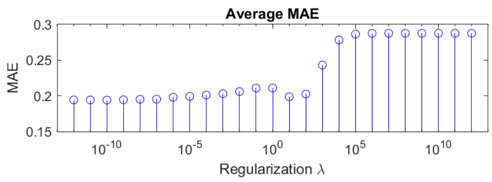

Figure 2: Average MAE for different λ

Consequently, error values for $\lambda \geq 10^6$ were excluded from further analysis. For sufficiently small λ, several window configurations achieved lower errors than the reconstruction using all available sub-frames equaling the complete frame. In the error metric plots, e.g. Fig. 3, this manifests as a distinct spike at the end where the full-signal reconstruction becomes suboptimal. This effect becomes increasingly pronounced as the regularization parameter decreases, indicating that lower values of λ amplify the sensitivity of the reconstruction to the specific set of sub-frames included.

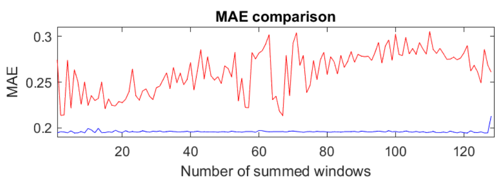

Figure 3: The MAE values resulting for reconstructing the signals using a window length of $L = 128$. In blue the errors for deconvolution using a regularization of $\lambda = 10^{-4}$, in red for $\lambda = 10^4$.

This behavior could be plausible given the structure of the inverse problem. Sub-frames in which the FFP passes through regions with little or no particle contribution add almost no useful information. Including them mainly introduces noise and systematic disturbances, which worsens the conditioning of the inverse problem. Excluding such low-information sub-frames therefore leads to a more stable reconstruction. In this reduced setting, a smaller regularization parameter is sufficient because the problem is restricted to a more informative spatio-temporal region.

IV. Conclusion

The results indicate that reduced data can yield improved reconstruction performance when the regularization parameter is sufficiently small, although this effect is likely to depend strongly on the specific phantom and its signal characteristics.

Future work could focus on identifying which sub-frames contribute meaningful information to the inverse problem. This may be achieved by analysing the signal energy or by incorporating knowledge of the FFP trajectory to distinguish informative from low-information sub-frames. Another approach could be analyzing the amplitude range of the sub-frame by comparing the minimum and maximum of the amplitude. Deciding whether a sub-frame should be reconstructed or not costs a small amount of time but that may be irrelevant as time is saved by not reconstructing all of the sub-frames. Such an approach could potentially reduce computational effort and reconstruction time while maintaining or even improving reconstruction quality. The procedure of sub-frame reconstruction may be advantageous in real measurements for dynamic structures or MPI scans using multi-patch measurement.

Acknowledgments

The work has been carried out at German Research Center for Artificial Intelligence (DFKI), Lübeck, Germany and supervised by the Institute of Medical Informatics, Universität zu Lübeck, Lübeck, Germany.

Author's statement

Conflict of interest: Authors state no conflict of interest.

References

[1] S. Bai, L. Gai, *et al.* Development of a human-size magnetic particle imaging device for sentinel lymph node biopsy of breast cancer. *Frontiers in Bioengineering and Biotechnology*, 12, 2024, doi:10.3389/fbioe.2024.1327521.

[2] T. Knopp and T. M. Buzug, Magnetic Particle Imaging: An Introduction to Imaging Principles and Scanner Instrumentation. Berlin/Heidelberg: Springer, 2012, doi:10.1007/978-3-642-04199-0.

[3] C. Brandt and C. Schmidt. Motion compensation for non-periodic dynamic tracer distributions in multi-patch magnetic particle imaging. *Physics in Medicine & Biology*, 67(8), 2022, doi:10.1088/1361-6560/ac5ce6.

[4] C. Droigk, M. Maass, *et al.* Direct multi-dimensional Chebyshev polynomial based reconstruction for magnetic particle imaging. *Physics in Medicine & Biology*, 67(4), 2022, doi:10.1088/1361-6560/ac4c2e.

[5] P. Vogel, S. Herz, *et al.* Low latency real-time reconstruction for MPI systems. *International Journal on Magnetic Particle Imaging*, 3(2), 2017, doi:10.18416/ijmpi.2017.1707002.